European Journal of Mechanics / A Solids 89 (2021) 104291

Contents lists available at ScienceDirect

European Journal of Mechanics / A Solids

journal homepage: http://www.elsevier.com/locate/ejmsol

Multiscale analysis and mechanical characterization of open-cell foams by simplified FE modeling

V.G. Belardi [a], P. Fanelli [b,*], S. Trupiano [a], F. Vivio [a]

[a] Department of Enterprise Engineering - University of Rome Tor Vergata, Via Del Politecnico, 1, 00133, Rome, Italy
[b] Department of Economics, Engineering, Society and Business Organization, University of Tuscia, Largo Dell'Università, 01100, Viterbo, Italy

ARTICLE INFO

Keywords:
Open-cell foam
Aluminum
Kelvin cell
FEA
Beam model
Experimental validation

ABSTRACT

Foam materials are experiencing a great diffusion in the industrial field because of their numerous properties and adaptability to different purposes. At the same time, research efforts are addressed to define new fields of application and methodologies of foam simulation, capable of combining their behavior at macroscale to phenomena at microscale, i.e. ligaments level. In this paper, a FE beam modeling strategy for open-cell foams acting on different scales of analysis is described. At first, on the microscale, the definition of the fundamental Kelvin unit cell is outlined with a particular characterization of the intersection zone between ligaments, that is a critical issue to obtain an accurate simulation instrument. The repetition of the unit cell within the material domain allows to obtain the overall foam material and operate at the macroscale. The elastic properties at macroscale are derived by means of FE analysis and compared with both solid model and experimental results. The proposed simplified FE modeling, using equivalent beam elements having suitable mechanical characteristics, demonstrates high accuracy levels and substantially relieve the computational efforts required by the commonly employed solid models.

1. Introduction

Nowadays the need for lightweight components with good mechanical properties and multifunctional characteristics is moving forward the limits in the use of classic metallic materials creating new kinds of applications, such as metal foams. Integrated design often requires individual components to perform multiple functions that can range from the structural field (Gong et al., 2005) to vibration isolation (Nguyen et al., 2019), up to the thermal field (Yang et al., 2020). Metal foams are very suitable for these purposes featuring a low apparent density, a high ratio of mechanical properties, in relation to their low density, and an excellent capacity to absorb shocks and vibrations.

The metal foams can be realized through a multitude of technological processes and materials, from the most advanced and expensive to the cheapest ones with high production capabilities (Ashby et al., 2000; Degischer and Brigitte, 2002; Kulshreshtha and Dhakad, 2020), such as mixing gas-realizing particles in the melt metal and 3D printing of the lattice structure (Plocher and Panesar, 2019).

In the last years, these porous materials have been utilized in many industrial fields. Principally, metal foams are used as filler material in sandwich panel. The scientific literature refers to their design and structural characterization (Wang et al., 2020), optimization under structural and thermal loads (Solyaev et al., 2019) and the dynamic behavior description of foam filled panels (Cheng et al., 2018). Moreover, the coexistence of stress states related to service loads and temperature field is often present in metal foam components. The mechanical behavior of open-cell aluminum foams subject to high temperature is experimentally investigated in (Aakash et al., 2019) where compressive loads were applied to foam specimens at several temperatures, it was found that the limit stress cannot only be related to the yield stress decrease of the base material, but also to a different crushing mechanism of the foam at high temperature. The foam material response is strongly related to the external loads and the subsequent crushing mechanisms of the open-cell foam, several works were realized to investigate complex loading condition such as quasi-static biaxial and triaxial loadings. In (Jung and Diebels, 2017) the macroscopic material behavior is studied under combined compression and torsional loads in order to obtain the yield surface for foams with different ppi value. Luo et al. (2018) report a study concerning the yield behavior of closed-cell aluminum foam performed through an image-based three-dimensional FE model, biaxial and triaxial compressive analyses are realized. Closed-cell foams were also investigated in (Dabo et al., 2019), a

* Corresponding author.
E-mail address: pierlugi.fanelli@unitus.it (P. Fanelli).

https://doi.org/10.1016/j.euromechsol.2021.104291
Received 4 December 2020; Received in revised form 26 January 2021; Accepted 10 April 2021
Available online 16 April 2021
0997-7538/

technique to develop the 3D FE model as a function of technological parameters is described. Then, the work by Yang and Kyriakides (2019) regards an experimental study regarding the crushing behavior of Al-alloy foams undergoing triaxial loadings. Also, the influence of the cutting method on the mechanical properties of the aluminum foams was assessed by Meng et al. (2019). Furthermore, the foam materials feature significant characteristics of energy absorption and thus are suitable for applications involving impact loadings. A relevant experimental campaign on impact testing of Al foams specimens is described in (Barnes et al., 2014; Gaitanaros and Kyriakides, 2014) determining the range of velocity for shock to occur. Additionally, in (Qi et al., 2018) the mechanical performance of a thin-walled beam with aluminum foam core utilized as bumper system for vehicle are studied and the load carrying capacity evaluation of circular sandwich plates with foam core is outlined in (Mao et al., 2016). Ref (Jin et al., 2019). discussed the effects of structural parameters on pyramidal kagome lattice material undergoing impact loading. Other potential scientific and industrial applications of this kind of material are currently in phase of study, such as the application of open-cell foams made of tungsten for the thermal protection in the nuclear fusion reactors (De Luca et al., 2019; De Luca et al., 2020; Muller et al., 2020; De Luca et al., 2021); the proposed tungsten foam protection is a sacrificial armor to reduce heat flux inside the tokamak reactors and to safeguard the cooling pipe system. In addition, foam materials feature a repeatable unit cell composing the overall domain; on a larger scale, the lattice structures present the same characteristic, such as the ones for aerospace applications (Belardi et al., 2018a, 2018b).

The real geometry modeling of open-cell foam is very difficult to achieve. Size and shape of cells and ligaments are not perfectly constant in the structure and many defects like voids, absence of ligaments or, conversely, solid cells or faces are present in the porous media. Many scholars developed systematic approaches to the analysis of foam materials. In (Jang et al., 2008) a modeling approach is realized by schematizing the foam structure as a pattern of regular Kelvin cells without defects and a comparison between a complex random foam microstructure and a regular Kelvin cell structure was realized; results showed the good accuracy of the proposed model. Elsayed and Pasini (2010) determined a multiscale criterion for the design of octet-truss lattice materials consisting in the proper design of the cell ligaments in order to raise the overall material buckling resistance, obtaining the instability collapse after the complete plasticization of the ligaments. In (Vigliotti and Pasini, 2012) different typologies of open and closed cell lattices are analyzed in terms of stiffness characterization, the analysis is structured on two scales: microscale, in order to determine buckling and yielding of the unit cell and, at macroscale level, the equivalent elastic properties of a continuum material are derived. In the framework of design methods for 3D printing products, Maskery et al. (2018) developed a methodology founded on finite element modeling for different surface-based lattice structures so as to determine their elastic properties, obtaining the relationships between elastic moduli and volume fraction. Similarly, the compressive behavior of additive manufactured steel lattice structures by means of finite element models realized with beam elements is investigated in (Guo et al., 2020). Duan et al. (2020) developed a topology optimization procedure to determine the unit lattice cell geometry capable of fulfilling different objectives; numerical and experimental analyses were performed to verify the properties of the printed lattice material specimens. An analytical derivation of mechanical properties of micro-lattice structures is presented in (Ptochos and Labeas, 2012) so as to obtain the three Young's Moduli and Poisson's ratios; in particular, the work is focused on a body centered cuboid cell and Timoshenko beam theory is employed to model the cell struts and derive the elastic response under complex loading. As regards the failure theories for 3D printed materials, Li et al. (2019) developed a multi-failure theory for hierarchical isogrid structures considering three possible failure modes related to material failure and local and global buckling which was verified by FE analyses. The elastic characterization of open-cell materials is realized in (Mao et al., 2020) through an inverse estimation method, based on the fitting of the displacement fields obtained through the application of compression and shear loads to a specimen in order to return as output an equivalent homogenized anisotropic material. Ren et al. (2019) outline a strategy aimed at stiffness improvement and stress concentration relief based on a reduction of sharp angles in the area of intersection between struts; a measurement of mechanical properties increase is reported. Yang et al. (2019) proposed an analytical methodology for the determination of foam-core sandwich structures, body-centered cubic unit cells are taken into account and the struts are modeled as Timoshenko beams, different deformation paths depending on the structure geometry are identified and the related elastic properties are derived. Furthermore, a regular Kelvin cell modeling of an aluminum open-cell foam with a low relative density was realized by Fanelli et al. (2017). Size and shape of ligament, node and cell were obtained from literature and original experimental evidences; a structural experimental foam characterization allowed the calibration of the model, realized by solid elements, that showed a good accuracy in stress field evaluation.

Despite the widespread applications and scientific literature about this topic, the structural modeling of foam materials remains an open problem because of the multiscale effects that affect the structural behavior of this class of materials. Metal foams with open cells and low apparent densities are used in real applications where external loads are almost exclusively of compression. In fact, in order to obtain the proper elastic response on macroscale, it is necessary to accurately consider the microscale geometry of the foam that is a critical issue from both the analytical point of view that from the numerical one. Indeed, finite element simulations of foam materials realized by solid elements are computationally onerous and simulation of big components of real engineering interest can become impossible to realize. For this reason, a FE model featuring beam elements is presented in this paper.

In this work, the presented beam finite element methodology for the analysis of open-cell foams exploits the characterization of the unit Kelvin cell. As outlined in (Jang et al., 2008; Fanelli et al., 2017), a regular disposition of this unit cell with averaged cross-section properties allows the simulation of the open-cells foam material, even if the actual distribution of ligaments and their cross-section is randomic. In addition, the Kelvin cells have a tetrakaidecahedron structure, the cross-section shapes of the cell edges are of prime importance to simulate the mechanical behavior of the foam materials (Gong et al., 2005; Jang et al., 2008). Additionally, the equivalent FE beam model is developed at the microscale so as to provide a Kelvin cell with an accurate modeling of the intersection node between ligaments, that is a crucial aspect to obtain the proper elastic characteristics of the model at the macroscale. The FE model stems from the ligament geometrical definition provided in (Fanelli et al., 2017). After the fundamental unit cell is defined, its repetition within the material domain allows to obtain the overall foam material and operate at the macroscale. The proposed simplified FE beam model, using equivalent beam elements having suitable mechanic characteristics, is verified against the outcomes of the solid FE model and the results of the experimental tests, performed in (Fanelli et al., 2017), showing a notable degree of agreement. Therefore, the simplified modeling allows to substantially relieve the computational efforts required by the commonly employed solid models, maintaining a high level of accuracy. Besides, the dependence of the elastic properties on the main geometrical variables and on the domain size is investigated through sensitivity analyses.

2. Experimental data

The FE beam model developed for open-cell foams is referred to the Al 6101-T6 Duocel® open-cell foam fabricated by ERG Aerospace Corporation with a pore density of 10 PPI. The experimental data, considered as comparison for the FE models, were achieved through experimental tests, as outlined in Fanelli et al. (2017).

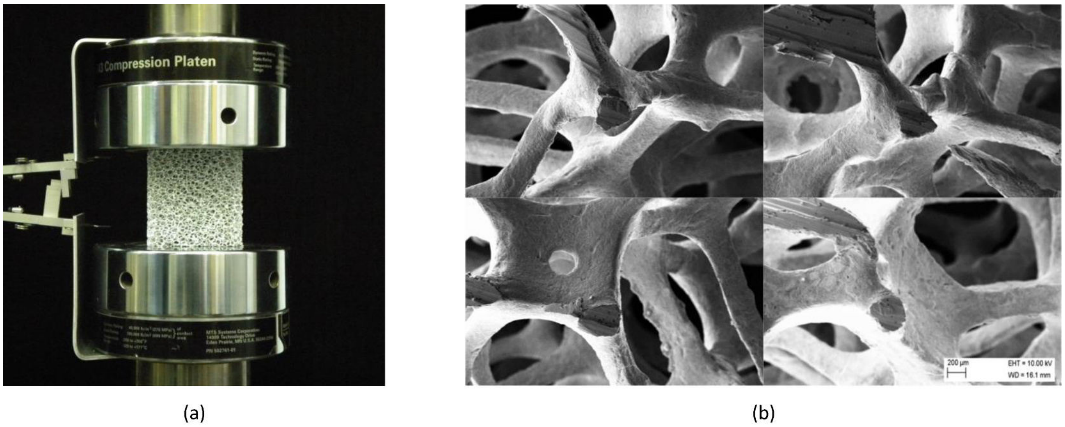

Fig. 1. (a) Compression test performed on the specimen of open-cell foam Al 6101-T6 Duocel® 10 PPI. (b) SEM magnifications of the specimen (Fanelli et al., 2017).

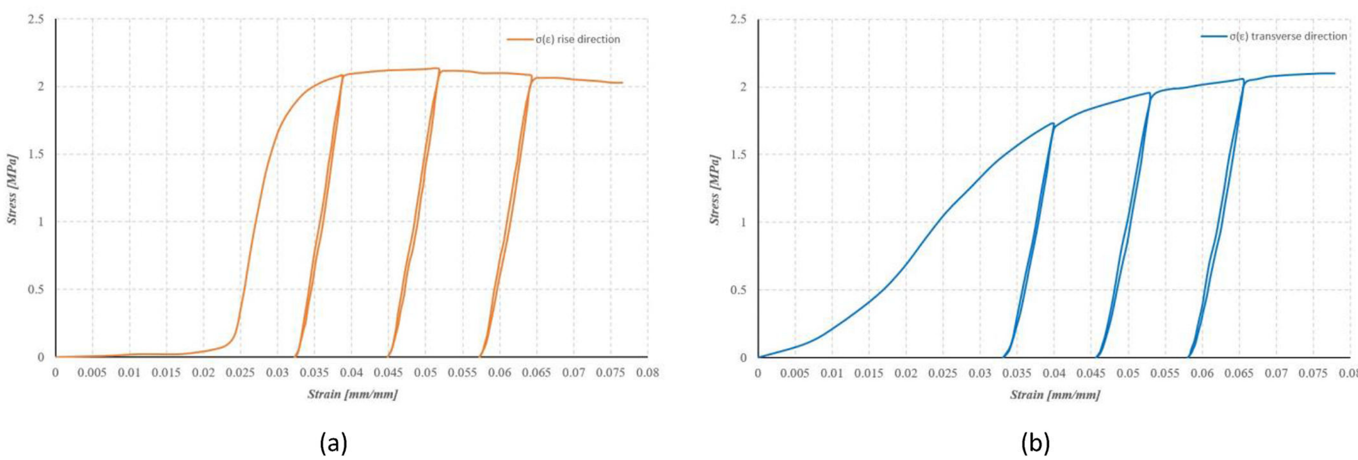

Fig. 2. Experimental stress-strain curve in the (a) rise and (b) transverse directions (Fanelli et al., 2017).

Table 1
Mean equivalent mechanical properties of Al-6101-T6 10 PPI foams in the rise and transverse directions (Fanelli et al., 2017).

E_{BM} [MPa]	E_y/E_{BM} [−]	E_x/E_{BM} [−]	ρ^0/ρ [%]	E_y [MPa]	E_x [MPa]	E_y/E_x [−]
69000	0.00497	0.00398	7.40	343.3	274.7	1.249

The structural response of the aluminum foams was determined by means of compression tests performed on specifically manufactured specimens with size 50 × 50 × 50 mm, using a customized tool composed of parallel platens and an axial extensometer, see Fig. 1(a). As in other open-cell foams, the Al 6101-T6 Duocel® is characterized by cells that are elongated on a preferential direction, i.e. the rise direction that is the anisotropy direction. The goal of the experimental campaign was measuring the equivalent moduli of elasticity in both the rise and the transverse directions; the rise direction is orthogonal to the platens in Fig. 1(a). Consequently, 4 uniaxial compression tests were realized along both the directions by means of an electromechanical testing machine with displacement control, the strain rate was 2.5 min^{-1}. The output of the test is showed in Fig. 2 with diagrams relating the strain and the equivalent stress, evaluated as the ratio between the machine crosshead load and the area of the specimen. The response of the material was observed by means of unloading and reloading sub-cycles during the compression test in the very first part of the curve, where the plateau behavior is at its beginning, in order to characterize the foam in undamaged conditions. Thus, the two equivalent moduli of elasticity were derived from the curves in Fig. 2.

Besides, the actual density of the foam specimens was further measured, it resulted to be equal to 7.4% in reference to the bulk aluminum.

The main experimental measures obtained with tests, here considered as a reference data, are reported in Table 1. E_{BM} is the Young's Modulus of the bulk material whereas E_y and E_x are the equivalent elastic moduli evaluated alongside both the rising and the transverse directions; ρ^0/ρ is the relative density of the foam with respect to the bulk aluminum.

Additionally, the experimental campaign allowed to characterize the foam microstructure through SEM images, depicted in Fig. 1(b), revealing that the ligaments are characterized by random features as regards their disposition in the unit cell and the geometrical properties (size and shape). In this regard, Jang et al. (2008), proposed the hypothesis that the ligaments cross-sections of Al foams feature equilateral triangular or circular shape, in order to obtain a regular geometry to build a FE model of the foam. Fanelli et al. (2017) further confirmed this hypothesis since the real shape observed is a compromise between the two possibilities. Therefore, the FE beam model hereafter described makes use of a repeatable unit cell, the Kelvin cell, with regular geometry based on the statistical characterization of the foam microstructure.

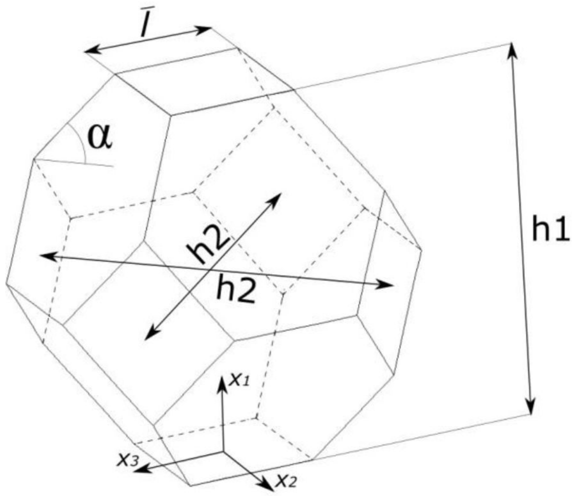

Fig. 3. Regular 14-sided polyhedron of Kelvin cell.

3. Foam FE beam models

The usual approaches to FE analysis of foams can be distinguished in reference to the use of beam or solid elements. As outlined in (Fanelli et al., 2017), the utilization of solid elements for the structural analysis is computationally onerous even if capable of returning remarkable insights of the foams elastic behavior. Nevertheless, the typical solid modeling capability of simulating three-dimensional effects cannot be appreciated by means of a simpler schematization, e.g. FE beam modeling.

The present investigation is focused on the development of a computationally efficient FE methodology founded on the employment of beam elements and this work represents a step forward with respect to the original solid FE modeling technique for open-cell foams presented and experimentally validated in (Fanelli et al., 2017). Hereafter, this solid model is considered as a reference term for a direct numerical comparison with the structural response of the beam model in order to obtain the correct calibration of the beam model.

Moreover, the developed FE beam model aims to define the influence of multiple aspects such as: (*i*) the cross-section area shape, (*ii*) the presence or absence of variation in section along the ligaments axis and (*iii*) the degree of anisotropy of the structure.

The FE beam models hereafter presented were designed to be perfectly periodic by adopting the regular 14-sided polyhedron of Kelvin cell (Fig. 3) that is capable of properly reproduce the elastic properties of an irregular foam, as discussed in (Jang et al., 2008). The geometry of the Kelvin cell is obtained considering the statistical distribution of the cells properties within the foam domain to obtain a representative fundamental unit cell.

The presented FE beam modeling strategy exploits the Kelvin cell as basic unit of the regular and repeatable scheme of the overall foam geometry; the beam elements feature an equilateral triangular or a circular cross-section for the foam ligaments (see Fig. 4) because, as stated by the manufacturer and confirmed in literature (Jang et al., 2008; Fanelli et al., 2017), the typical experimental values of relative density between 8% and 9% involve rounded convex cross-sections, such as the aforementioned geometries. Consequently, 3 K cell FE beam models characterized by different cross-section shape features were compared:

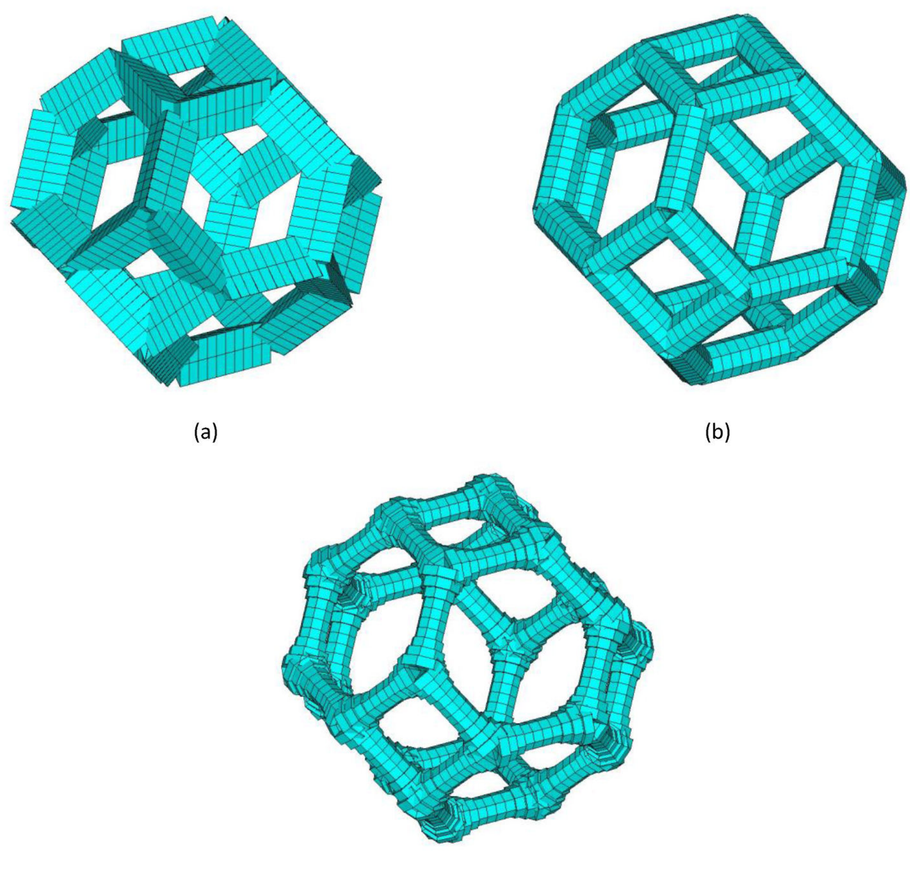

Fig. 4. The FE beam models of the Kelvin cell: (a) triangular cross-section model, (b) circular cross-section model and (c) circular cross-section with discrete variation along the ligaments.

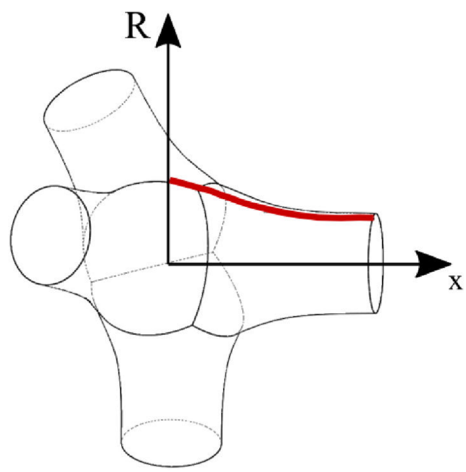

Fig. 5. Actual ligament profile of open-cell foams.

Table 2
Geometrical features of the constant triangular and circular ligaments cross-section.

Constant discrete profile		
A [mm^2]	a [mm]	R [mm]
0.340	0.886	0.329

Table 3
Geometrical features of the variable circular cross-section FE beam model.

Variable discrete profile			
Division	$x/\bar{l}$	R [mm]	A [mm^2]
1	$0.0\leq x/\bar{l} <0.1$	0.414	0.538
2	$0.1 \leq x/\bar{l} < 0.2$	0.343	0.370
3	$0.2 \leq x/\bar{l} < 0.3$	0.281	0.248
4	$0.3 \leq x/\bar{l} \leq 0.7$	0.244	0.187
5	$0.7 < x/\bar{l} \leq 0.8$	0.281	0.248
6	$0.8 < x/\bar{l} \leq 0.9$	0.343	0.370
7	$0.9 < x/\bar{l} \leq 1.0$	0.414	0.538

- Triangular cross-section area, Fig. 4(a)
- Circular cross-section area, Fig. 4(b)
- Circular cross-section area with discrete variation along the ligaments, Fig. 4(c)

More elaborate modeling solutions, such as the employment of custom beam elements (Vivio, 2009; Belardi et al., 2021), could also be employed; anyway, the aforementioned models are simpler and can be easily implemented in the main FE software packages.

The theoretical framework behind the proposed FE beam modeling approach is based on the strategy proposed in (Fanelli et al., 2017) for the solid model methodology. This approach prescribes a variable radius along the ligament axis obtained with the analytical modeling of the ligament shown in Fig. 5. The ligament is described through a function of the cross-section area radius; in particular, the radius R is expressed, as a polynomial function, depending on the abscissa x evaluated alongside the ligament axis and normalized in respect to the length of ligament $\bar{l}$:

$$R\left(\frac{x}{\bar{l}}\right) = -19.427\left(\frac{x}{\bar{l}}\right)^6 + 58.282\left(\frac{x}{\bar{l}}\right)^5 - 66.198\left(\frac{x}{\bar{l}}\right)^4 + 35.261\left(\frac{x}{\bar{l}}\right)^3 - 7.8969\left(\frac{x}{\bar{l}}\right)^2 - 0.02\left(\frac{x}{\bar{l}}\right) + 0.4336 \tag{1}$$

Furthermore, the FE beam modeling makes use of the anisotropy factor λ of the structure, defined in (Fanelli et al., 2017), which is determined by means of the rotation of the ligaments with projection in the x_1-direction, but maintaining them unchanged in terms of length:

$$\lambda = \frac{h_1}{h_2} = \frac{4l\sin(\alpha)}{2l\cos\left(\frac{\pi}{4}\right) + 2l\cos(\alpha)} = 4\frac{\sqrt{1-\cos^2(\alpha)}}{\sqrt{2}+2\cos(\alpha)} \tag{2}$$

In addition, the parametric coordinates of the nodes of connection for a singular cell affected by a given anisotropy factor λ are defined by the angle of projection α obtained as:

$$\alpha = \arccos\left(-\frac{0.707}{4+\lambda^2}\lambda^2 + \frac{\sqrt{2\lambda^2+16}}{4+\lambda^2}\right) \tag{3}$$

The cross-section area value of the FE beam models with constant circular and equilateral triangular cross-section is defined on the basis of the mean value of the function defining the area variation, in order to obtain a beam structure comparable with the solid model, that in turn was derived from the experimental evidence. Subsequently, the constant value of cross-section area A is obtained as:

$$A = \int_0^1 \pi R^2\left(\frac{x}{\bar{l}}\right) d\left(\frac{x}{\bar{l}}\right) \tag{4}$$

Once the constant area value is determined, the geometrical properties of both the circular and the triangular cross-sections, i.e. the side of the equilateral triangle a and the radius of circle R, can be defined these values are reported in Table 2. Besides, considering an isotropic foam-domain, the cell dimension is equal to $h_1 = h_2 = 2\sqrt{2}l$ for all the three directions. With reference to the ligaments with triangular cross-section, the orientation of the cross-section was deduced from the experimental investigation (see Fig. 1(b)). The orientation is different for the oblique ligaments and for those shared by different unit cells. In the first case, the triangular cross-sections were oriented with the vertex pointing outside the unit cell, and the opposite side of the triangle is orthogonal to line joining the vertex and the barycenter of the unit cell. The ligaments shared by multiple unit cells form a square profile, the vertex of the triangular section points towards the center of the square and lays on it. This solution allows for the repeatability of the unit cell.

As regards the FE beam model with variable cross-section, the variation of the cross-section area was obtained by subdividing the ligament in discrete segments and assigning to the N divisions of the ligament different values of area, i.e. the generic *i-th* division of the ligament features an area A_i and a radius R_i. In particular, the determination of the cross-section geometrical properties of the N divisions of the ligament profile was performed by means of Eq. (5); the cross-section area A_i was obtained by the multiplication between the mean length value integral of the *i-th* division and the value of minimum area A_0:

$$A_i = \frac{1}{\bar{L}_i - \bar{L}_{i-1}} \int_{\bar{L}_{i-1}}^{\bar{L}_i} \pi R^2\left(\frac{x}{\bar{l}}\right) d\left(\frac{x}{\bar{l}}\right) \tag{5}$$

where L_i and L_{i-1} are the values of the dimensionless abscissa delimiting the *i-th* division that composes a segment of the ligament.

The length of each division was considered to be inversely proportional to the magnitude of variation of the function $R(x/\bar{l})$; this allowed to obtain a better fitting between the discrete profile and the continuous

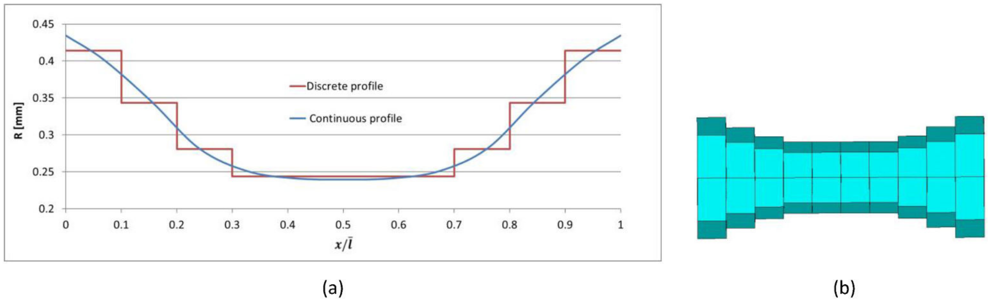

Fig. 6. (a) Difference between the continuous and the discrete ligaments profile. (b) Ligament of the beam elements modeling.

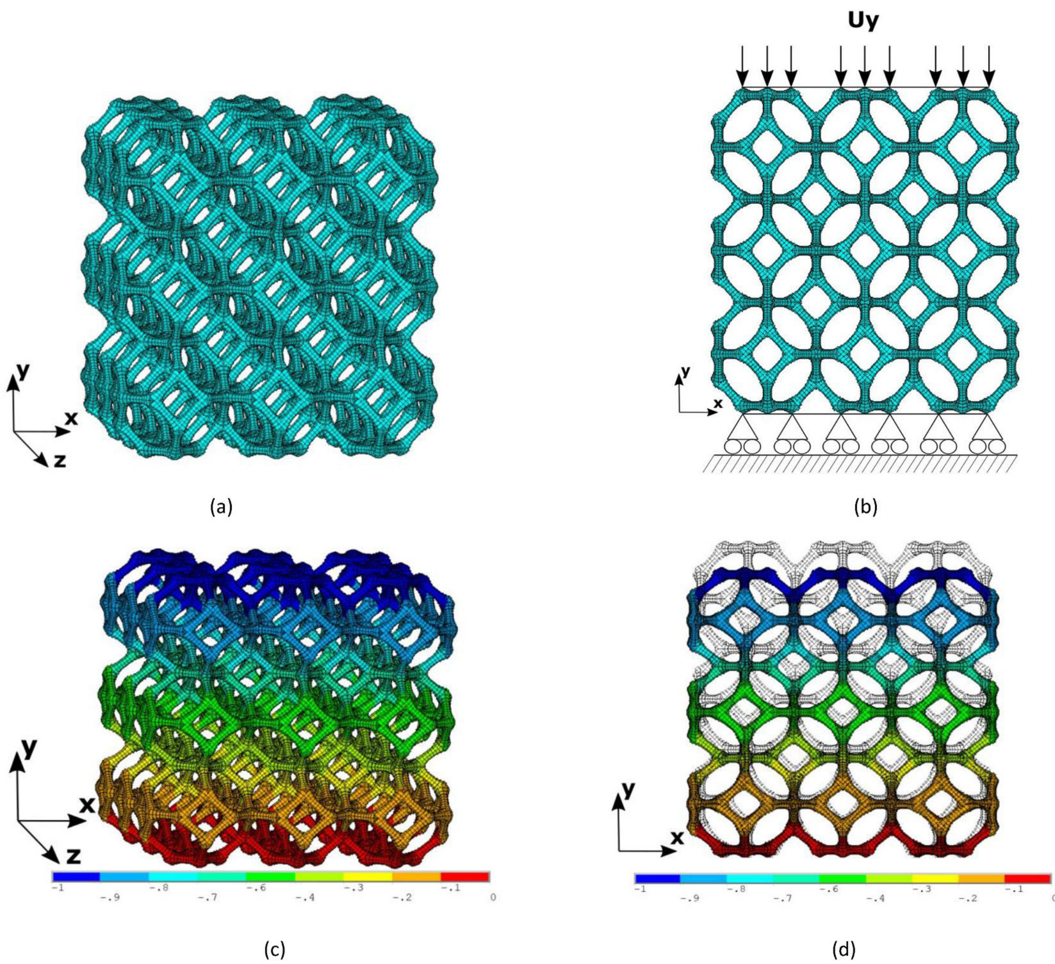

Fig. 7. (a) $3 \times 3 \times 3$ foam domain of a circular cross-section with discrete variation along the ligaments model; (b) boundary conditions: imposed displacement on top face and simply supported lower face. Contour of y-displacement: (c) prospective and (d) front view with undeformed model.

one.

The comparative analysis of the FE beam models with different cross-section presented in the following Section was performed with 7 discrete values of the cross-section area per ligament, this value was obtained by means of a convergence analysis of the mesh. In this regard, Table 3 outlines the values of the discrete area A_i and radius R_i, calculated according to the presented method, and it further reports the $x/\bar{l}$ divisions extension. Near the ends of the ligament the variation of the cross-section area is considerable and an adequate discretization is needed; in fact, all divisions except the 4-th, features a $\overline{L}_i = 0.4$. The 4-th division has an extension $\overline{L}_i = 0.4$ because in this zone, close to the central zone of the ligament, the gradient of.

$R(x/\bar{l})$ is very flat. The variation of ligaments profile is showed in Fig. 6(a), the blue curve represents the continuous profile of the ligament used for the solid modeling outlined in (Fanelli et al., 2017), whereas the red one shows the resulting discrete profile of the beam modeling.

Additionally, in order to realize beam elements featuring the same length, with evenly spaced nodes along the ligament, the 4-th division is composed of 4 beam elements meanwhile the other divisions present one element. In this way the ligament is composed of 10 beam elements with the same length. Fig. 6(b) shows the resulting ligament of the beam model.

Moreover, a further characteristic of the foam FE beam modeling technique is the capability of considering the anisotropy of the structure; therefore, both isotropic and anisotropic foams can be modeled. As

Table 4
Comparison of F_y [N] force reactions of foam FE beam models.

	TCI	CCI	CVI	CCA	CVA	Solid model
F_y [N]	3291.57	2974.17	3517.87	4221.45	4901.57	4955.87

Table 5
Percentage difference of ΔF_y [%] force reactions between the foam FE beam models and the solid model.

	TCI	CCI	CVI	CCA	CVA
ΔF_y [%]	−33.58	−39.99	−29.02	−14.82	−1.10

previously discussed, the anisotropy factor λ is related to the angle of projection in the x_1-direction, i.e. α. Since the anisotropy only influences the ligaments orientation, and it does not affect their profile, the evaluation of cross-section properties is the same for the realization of both isotropic and anisotropic models. Conversely, the difference lies in the proportions of the unit cell; in fact, the anisotropic unit cell features a stretched morphology characterized by unit cell dimensions: $h_1 = 4l\sin(\alpha)$ along the anisotropy direction, and $h_2 = 2l\cos(\pi) + 2l\cos(\alpha)$ along the other two directions.

4. Comparison of FE beam models

This Section concerns a comparative study of the foams FE beam models in terms of structural response of a cubic foam domain consisting of $3 \times 3 \times 3$ Kelvin cells. The comparison regarded the stiffness of the FE beam models, a compressive stress state was induced in the foam domain: the lower face, parallel to the xz-plane was simply supported whereas a unitary displacement was applied to the upper face, i.e. along the y-direction (see Fig. 7). Then, the FE models stiffness values were evaluated through the ratio between the reaction force and the imposed displacement.

All the FE models are characterized by ligaments with the same length. Two-noded linear shear deformable beam elements with 6 DOFs per node were employed for the mesh generation; the FE beam models utilized for these analyses featured 36 ligaments, 440 elements, 348 nodes for a total amount of 2088 DOFs.

The base material was assumed to be linear elastic with Young's Modulus $E_{BM} = 69000$ MPa, Poisson's ratio $\nu = 0.30$ and density of the base material $\rho = 2690$ kg/m^3.

The presented case study regarded the following typologies of foam FE beam models:

- Triangular constant cross-section isotropic (TCI)
- Circular constant cross-section isotropic (CCI)
- Circular variable cross-section isotropic (CVI)
- Circular constant cross-section anisotropic (CCA)
- Circular variable cross-section anisotropic (CVA)

Furthermore, it should be noted that a rigorous stiffness comparison requires the same dimensions of the overall domains. Anyway, the geometrical equivalence between anisotropic and isotropic domains is not perfectly respected since the upper loaded section area of the anisotropic domain is less extended than the isotropic one, whereas its size in the load direction is slightly superior. These differences are due to the ligaments parameterization of anisotropy that conserves their lengths.

Taking into account the results of the force resultants F_y reported in Table 4, some of conclusions reported in (Jang et al., 2008) can be further confirmed even if obtained with a different geometrical parametrization. In fact, the TCI model turned out to be stiffer with respect to the CCI model and the difference in terms of elastic response cannot be considered negligible (see Table 5). Moreover, the non-constant cross-section model and the anisotropic model are characterized by a more similar behavior to the solid model. Additionally, it should be noted that the superposition between the non-constant cross-section and the anisotropy, i.e. the CVA FE model, is responsible of a percentage variation very low in reference to the solid model.

Finally, the usage of the CVA model, that features the anisotropic Kelvin cell geometry with discrete circular cross-section ligament, can be considered the most suitable solution for FE beam modeling. In fact, as outlined in Table 5, the CVA model features a reaction force F_y closer to the solid one. Besides, this model is more adherent to the actual ligaments geometry, thus it can more accurately replicate its structural behavior, the equivalent density that is one of the fundamental parameters of porous materials, and it could more easily bring to a dynamic calibration. Further, this variant of the FE beam model is characterized by higher margins of calibration in order to obtain the desired elastic properties and allows for the direct comparison with the solid model presented in (Fanelli et al., 2017) that makes use of analogous geometrical parametrization.

5. Comparison of elastic response between beam and solid models

With respect to the computational cost of numerical simulations, solid modeling is more onerous than the beam one. However, a solid model can reproduce the effects linked to the triaxiality of the stress state and the stress concentration in the area of mutual intersection between ligaments. An intersection point of four concurrent ligaments is named as connection node, as shown in Fig. 8 (a). Therefore, considering the relevant influence of the connection nodes on the overall foam domain, a first comparison between the two types of FE models was performed through the analysis of a single connection node. The outcomes of this comparative analysis were utilized to draw a preliminary

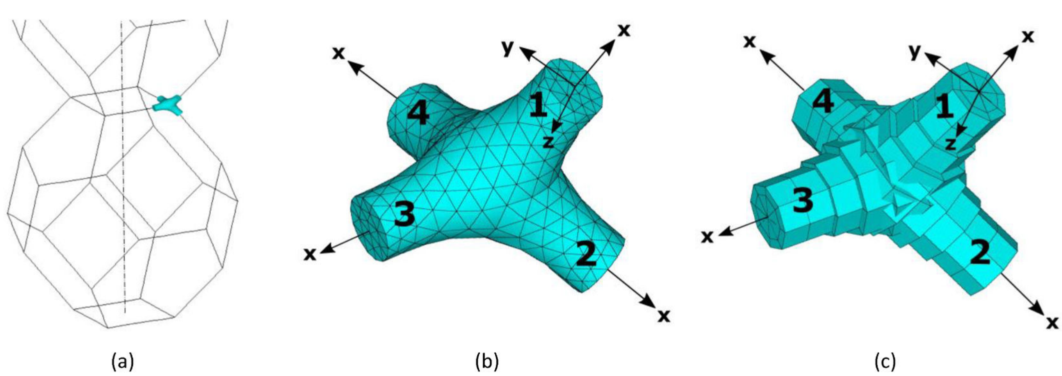

Fig. 8. (a) A connection node between two cells composed of four ligaments, (b) a connection node meshed realized with solid elements, (c) a connection node realized with beam elements.

Table 6
Stiffness table [N/mm] of connection node solid model.

K^s	u_x^1	u_y^1	u_z^1	u_x^2	u_y^2	u_z^2	u_x^3	u_y^3	u_z^3	u_x^4	u_y^4	u_z^4
F_x^1	9513	−281	0	2611	2122	0	4031	832	1719	4029	832	−1720
F_y^1	−281	2512	0	2125	1168	0	−898	−129	−428	−897	−129	427
F_z^1	0	0	2082	0	0	158	−1754	−394	−674	1753	393	−674
F_x^2	2611	2125	0	9506	−278	0	4025	828	−1716	4028	830	1717
F_y^2	2122	1168	0	−278	2510	0	−896	−128	426	−897	−129	−427
F_z^2	0	0	158	0	0	2076	1747	392	−671	−1749	−392	−672
F_x^3	4031	−898	−1754	4025	−896	1747	9420	243	0	2079	−2147	0
F_y^3	832	−129	−394	828	−128	392	243	2524	0	−2149	1243	0
F_z^3	1719	−428	−674	−1716	426	−671	0	0	2146	0	0	203
F_x^4	4029	−897	1753	4028	−897	−1749	2079	−2149	0	9423	243	0
F_y^4	832	−129	393	830	−129	−392	−2147	1243	0	243	2523	0
F_z^4	−1720	427	−674	1717	−427	−672	0	0	203	0	0	2148

Table 7
Percentage difference [%] between stiffness tables obtained with beam and solid models.

ΔK^{bs}	u_x^1	u_y^1	u_z^1	u_x^2	u_y^2	u_z^2	u_x^3	u_y^3	u_z^3	u_x^4	u_y^4	u_z^4
F_x^1	−11.6	−1.8	0.0	−1.2	−15.5	0.0	−2.2	−6.1	−11.6	−2.2	−6.1	11.6
F_y^1	−0.5	−16.6	0.0	−4.1	−12.0	0.0	1.8	0.0	4.1	1.7	0.0	−4.1
F_z^1	0.0	0.0	−10.5	0.0	0.0	0.9	2.6	3.2	4.7	−2.6	−3.2	4.7
F_x^2	−1.2	−15.6	0.0	−11.6	−2.0	0.0	−2.1	−6.0	11.4	−2.2	−6.1	−11.5
F_y^2	−4.1	−12.0	0.0	−0.5	−16.5	0.0	1.7	−0.1	−4.0	1.7	0.0	4.1
F_z^2	0.0	0.0	0.9	0.0	0.0	−10.2	−2.5	−3.1	4.6	2.6	3.1	4.6
F_x^3	−2.2	6.6	11.9	−2.1	6.5	−11.6	−11.9	3.3	0.0	−1.1	16.2	0.0
F_y^3	−1.6	0.0	3.9	−1.6	−0.1	−3.8	0.9	−17.6	0.0	4.4	−13.6	0.0
F_z^3	−2.6	3.5	4.9	2.6	−3.4	4.7	0.0	0.0	−10.9	0.0	0.0	0.5
F_x^4	−2.1	6.5	−11.8	−2.1	6.5	11.7	−1.1	16.3	0.0	−11.9	3.3	0.0
F_y^4	−1.6	0.0	−3.8	−1.6	0.0	3.8	4.3	−13.6	0.0	0.9	−17.6	0.0
F_z^4	2.6	−3.5	4.9	−2.6	3.5	4.8	0.0	0.0	0.5	0.0	0.0	−10.9

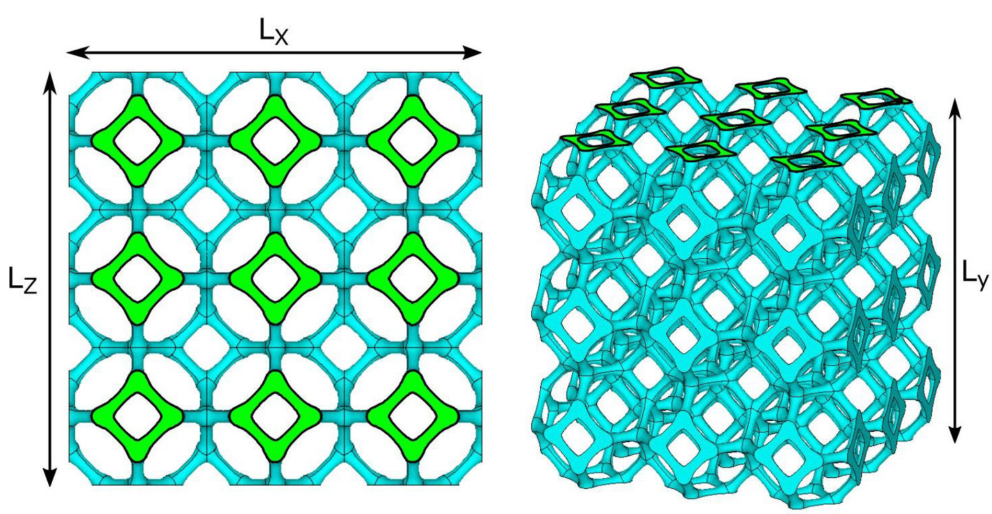

Fig. 9. Dimensions of a 3 × 3 × 3 cells foam domain.

conclusion about the structural behavior of the FE beam model and outline a corrective strategy.

The results of the proposed FE beam modeling technique were compared in terms of accuracy and validity against the ones obtained with the FE solid models described in (Fanelli et al., 2017). Fig. 8 (b) and (c) report the FE models of the ligaments connection node modeled with solid and beam elements, respectively; the ligaments extremities are numbered in order to identify them. Moreover, the FE beam model was realized with two-noded beam elements featuring 6 DOFs per node, whereas the FE solid model was meshed with tetrahedral ten-noded solid elements with 3 DOFs per node.

The four ligaments composing the connection node feature a local

Table 8
Equivalent Young's Moduli of beam model. Solid model results from Ref. (Fanelli et al., 2017).

	E_y [MPa]	E_x [MPa]	E_y/E_x [−]
Beam model	306.3	244.1	1.255
Solid model	351.8	281.2	1.251
Δ beam-solid [%]	−12.92	−13.20	0.32

Table 9
Comparison between the equivalent Young's Moduli obtained with FE beam model and solid model (Fanelli et al., 2017).

Domain [Cells]	E_y [MPa]	E_x [MPa]	Ey/Ex [−]	ΔE_y beam-solid [%]	ΔE_x beam-solid [%]	$\Delta E_y/E_x$ beam-solid [%]
6 × 6 × 6	308.0	246.7	1.248	−12.45	−12.26	−0.24
9 × 9 × 9	308.0	247.1	1.247	−12.44	−12.12	−0.32
12 × 12 × 12	308.9	248.0	1.246	−12.20	−11.81	−0.40

Cartesian coordinate system oriented as follows:

- x-axis oriented normal to the ligament section.
- y-axis lying in the section plane and oriented towards the barycentric axis of the cell in the anisotropy direction (dashed line in Fig. 8 (a)).
- z-axis determined according to the right-hand rule.

The comparison of the solid and beam models connection node is realized in terms of stiffness table, as the one reported in Table 6 for the solid model. In particular, each stiffness value is obtained imposing to the four ligaments end a unitary translation displacement, sequentially, along the x-, y- and z-direction of the local coordinate systems. Meanwhile the unitary displacement was applied to a single degree of freedom of one ligament, a system of constraints was imposed to the other degrees of freedom of the four ligaments free faces, restraining the translations. To make the comparison consistent, the rotational degrees of freedom of the FE beam model were further fixed. Then, the ratio between the forces measured in the four ligaments ends and the applied displacement returns the stiffness value.

Consequently, a total of 12 distinct displacements were alternatively applied along the three Cartesian directions of the four ligaments and the corresponding 12 forces were evaluated. One of these forces is associated with the applied displacement, the remaining ones are the reaction forces to maintain the equilibrium. The resultant forces F_x, F_y and F_z were evaluated in the respective local coordinate system.

With regard to the stiffness values obtained for the solid model reported in Table 6, the 3 × 3 sub-tables related to a single ligament present comparable values, denoting similar stiffness properties of the four ligaments.

Furthermore, Table 7 shows the percentage difference of the connection node beam model stiffnesses compared to the solid model. In order to emphasize the stiffness values with higher magnitude, that as a consequence are more influential on the resulting elastic properties, the values of the percentage difference are evaluated with reference to the higher stiffness on each column, i.e. the one on the main diagonal:

$$\Delta K_{ij}^{bs} = 100\,\frac{K_{ij}^{b} - K_{ij}^{s}}{K_{ii}^{s}} \tag{6}$$

For the most part, the values reported in Table 7 are negative. The few results where the stiffness values of the beam model are higher than the solid model ones are, in general, very low if compared to the stiffnesses related to the applied displacements. Such stiffnesses are shown on the main diagonal of Table 6. Neglecting the few secondary positive

Table 10
Percentage difference $\mathbf{\Delta K^{bs}}_{ii}$ between stiffness tables obtained with during the minimization process.

	$F = 1.0$	$F = 1.5$	$F = 2.0$	$F = 2.5$
ΔK_{11}^{x}	−11.63	−7.88	−5.88	−4.61
ΔK_{11}^{y}	−16.60	−12.22	−9.75	−8.24
ΔK_{11}^{z}	−10.47	−6.15	−3.75	−2.26
ΔK_{22}^{x}	−11.56	−7.82	−5.81	−4.54
ΔK_{22}^{y}	−16.53	−12.15	−9.68	−8.17
ΔK_{22}^{z}	−10.21	−5.88	−3.47	−1.97
ΔK_{33}^{x}	−11.88	−8.10	−6.07	−4.80
ΔK_{33}^{y}	−17.59	−13.27	−10.86	−9.31
ΔK_{33}^{z}	−10.86	−6.43	−4.01	−2.47
ΔK_{44}^{x}	−11.91	−8.13	−6.10	−4.83
ΔK_{44}^{y}	−17.56	−13.24	−10.82	−9.27
ΔK_{44}^{z}	−10.94	−6.52	−4.10	−2.56

Table 11
Comparison between the equivalent Young's Moduli obtained with FE beam model and solid model (Fanelli et al., 2017).

F [−]	E_y [MPa]	E_x [MPa]	Ey/Ex [−]	ΔE_y beam-solid [%]	ΔE_x beam-solid [%]	$\Delta E_y/E_x$ beam-solid [%]
1.0	306.3	244.1	1.255	−12.93	−13.19	0.30
1.5	325.4	259.4	1.254	−7.50	−7.75	0.27
2.0	336.0	267.9	1.254	−4.49	−4.73	0.26
2.5	342.7	273.4	1.253	−2.59	−2.77	0.20

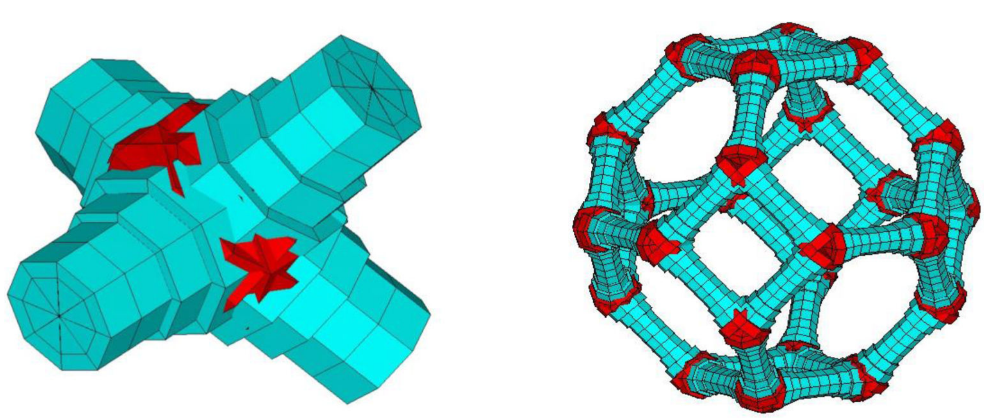

Fig. 10. Young's Modulus increment for the ligament segment adjacent to the connection node.

Table 12
Percentage difference [%] between stiffness tables of calibrated beam with $F = 2.5$ and solid models.

ΔK^{bs}	u_x^1	u_y^1	u_z^1	u_x^2	u_y^2	u_z^2	u_x^3	u_y^3	u_z^3	u_x^4	u_y^4	u_z^4
F_x^1	−4.6	−2.9	0.0	−0.5	−8.2	0.0	−0.1	−3.2	−4.7	−0.1	−3.2	4.7
F_y^1	−0.8	−8.2	0.0	−2.2	−6.8	0.0	0.9	−0.9	1.8	0.9	−0.9	−1.7
F_z^1	0.0	0.0	−2.3	0.0	0.0	2.1	1.0	1.3	0.4	−1.0	−1.3	0.4
F_x^2	−0.5	−8.3	0.0	−4.5	−3.0	0.0	0.0	−3.0	4.5	0.0	−3.1	−4.6
F_y^2	−2.2	−6.8	0.0	−0.8	−8.2	0.0	0.9	−1.0	−1.7	0.9	−0.9	1.7
F_z^2	0.0	0.0	2.1	0.0	0.0	−2.0	−1.0	−1.3	0.2	1.0	1.3	0.3
F_x^3	−0.1	3.3	4.7	0.0	3.3	−4.3	−4.8	4.3	0.0	−0.7	9.1	0.0
F_y^3	−0.8	−0.9	1.6	−0.8	−1.0	−1.5	1.1	−9.3	0.0	2.5	−8.2	0.0
F_z^3	−1.1	1.5	0.4	1.0	−1.4	0.2	0.0	0.0	−2.5	0.0	0.0	1.9
F_x^4	−0.1	3.3	−4.6	0.0	3.3	4.4	−0.7	9.2	0.0	−4.8	4.3	0.0
F_y^4	−0.8	−0.9	−1.6	−0.8	−0.9	1.5	2.4	−8.2	0.0	1.1	−9.3	0.0
F_z^4	1.1	−1.5	0.4	−1.0	1.5	0.3	0.0	0.0	1.9	0.0	0.0	−2.6

Table 13
3 × 3 × 3 foam domain: equivalent Young's Moduli of calibrated beam model with $F = 2.5$ and experimental results.

	E_y [MPa]	E_x [MPa]	Ey/Ex
Beam model	342.7	273.4	1.253
Experimental	343.3	274.7	1.249
Δ beam-exp. [%]	−0.16	−0.48	0.31

forces aforementioned, these results demonstrate a stiffer behavior of the solid model then the one of the beam model, as expected.

Moreover, a comparative study was also realized considering foam domains made of multiple cells. As reported in (Fanelli et al., 2017), a very useful index for the characterization of the stiffness of a cellular domain is the equivalent modulus of elasticity. This index is not only a function of the Young's Modulus of the material, but also of the complete mechanical behavior due to the microstructural set of ligaments and nodes that characterizes the cell domain. Two elastic moduli can be defined for the anisotropic foams: E_y in the anisotropy direction and E_x measured along one of the other two directions. The equivalent moduli of elasticity are obtained through a FE elastic static analysis characterized by an imposed displacement applied on the top surface of the foam domain, whereas the opposite surface is constrained along the direction of the imposed displacement.

The equivalent modulus of elasticity E_y along the y-direction is defined by the following expression:

$$E_y = \frac{\sigma_y}{\varepsilon_y} = \frac{F_y}{A_{xz}} \frac{L_y}{\Delta_y} \tag{7}$$

where: the equivalent cross-section A_{xz} is obtained through the product of L_x and L_z (see Fig. 9), Δ_y is the length variation of the overall foam domain along the y-direction that coincides with the displacement imposed. The other equivalent modulus is analogously calculated in the x-direction. Moreover, it should be noted that the equivalent modulus in z-direction coincides with the one in the x-direction.

A comparison reporting the equivalent elastic moduli of the 3 × 3 × 3 beam model domain and of the solid model, derived from Fanelli et al. (2017), is shown in Table 8. Other comparisons in terms of equivalent elastic moduli of foam domains with different number of Kelvin cells, obtained with the proposed beam model and the solid model, are reported in Table 9. The equivalent moduli of elasticity revealed a lower stiffness of the beam model with respect to the solid one. This phenomenon was quite similar for the elastic moduli evaluated in both y- and x-direction. As confirmation of this statement, the E_y/E_x ratio of the two FE models are very close.

These last results, obtained with large domains, clearly corroborate the trend determined with the analysis of connection node in terms of reduced stiffness of the FE beam model with respect to the solid one. Nevertheless, the importance of the elastic simulation of the connection node is more clearly shown in the next Section; indeed, by means of its calibration the divergence between beam and solid models are remarkably reduced.

6. FE beam model calibration

The intrinsic characteristics of the FE beam modeling are responsible for the difference between the structural behavior between the two modeling strategies. In fact, the three-dimensional features of the connection node between ligaments are not directly reproduced by the beam model. Conversely, the connection node modeled with solid elements is representative of the actual geometry of the intersection zone, even though the computational efforts for the FE solid analysis are remarkably higher. Keeping in mind the capabilities of the FE beam modeling, this methodology requires a preliminary calibration to adjust the model parameters and more properly simulate the structural behavior of a foam domain. In this order of ideas, since the solid model presented in Fanelli et al. (2017) demonstrated a good accuracy with respect to the experimental results, the calibration of the beam model was performed with reference to the solid model. In particular, scope of the present study is demonstrating the feasibility of the beam model calibration. It is focused on the correction of the connection node elastic properties in order to obtain the overall agreement between the beam and solid models in terms of compressive behavior along both the y- and the x-directions.

Furthermore, the calibration process was performed on the FE model with ligaments featuring circular cross-section with discrete variation CVA. Following to some configuration tests, it was determined that the adjustment capable of returning the FE beam model calibration is the Young's Modulus increment of the ligament segment adjacent to the connection node, highlighted in red in Fig. 10. This strategy allowed to obtain the elastic equivalence with the compressive behavior of the solid model. A measure of the Young's Modulus variation is the scaling factor F defined as the ratio between the ligament connection node modified Young's Modulus E^* and the base material one, i.e. $E_{BM} = 69000$ MPa:

$$F = \frac{E^*}{E_{BM}} \tag{8}$$

During the calibration process, the parameter F was varied to minimize the percentage difference in Table 7 between the stiffness tables of

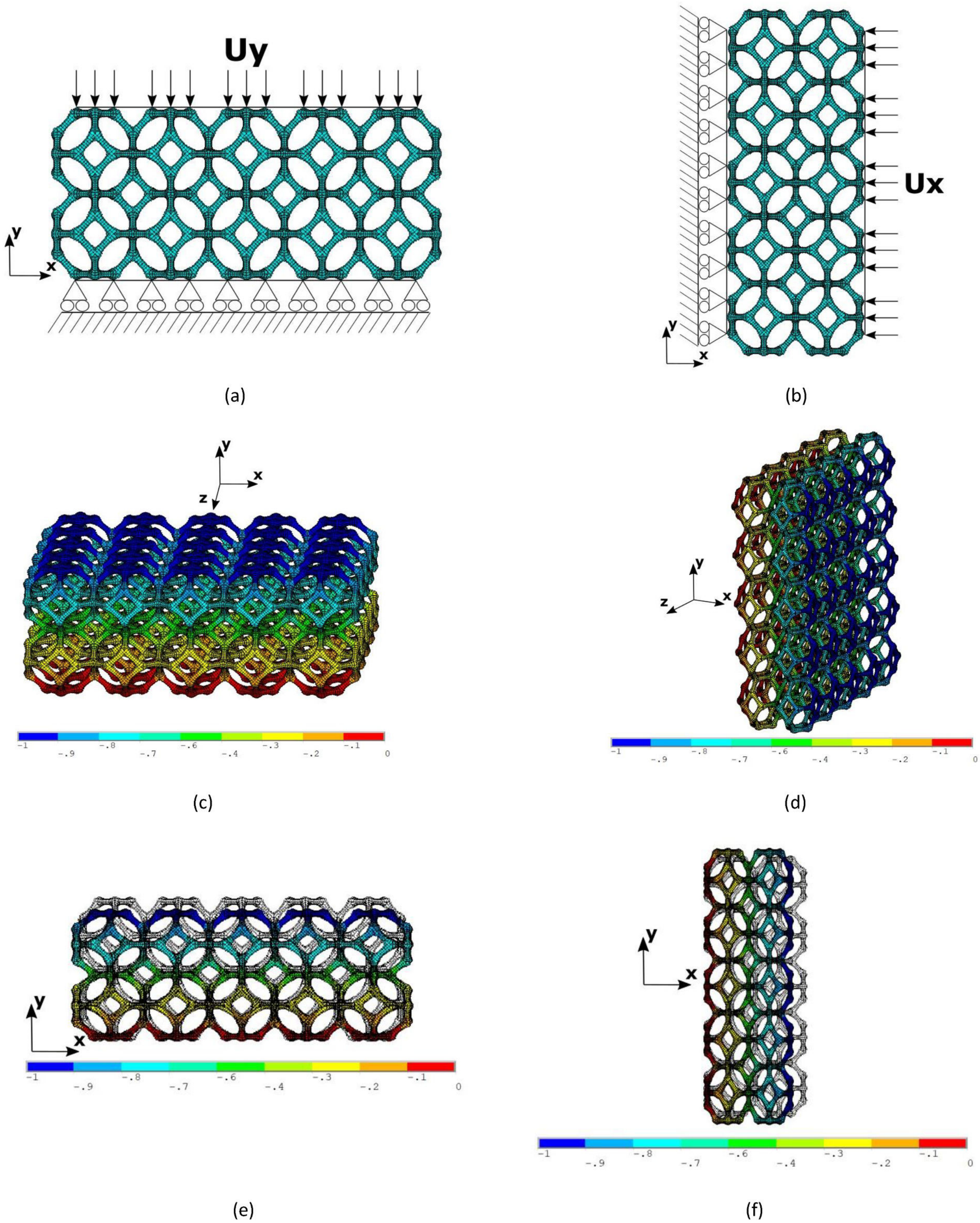

Fig. 11. E_y evaluation on a 5 × 2 × 5 domain: (a) boundary conditions, (c) and (e) contour of y-displacement. E_x evaluation on a 2 × 5 × 5 domain: (b) boundary conditions, (d) and (f) contour of *x*-displacement.

Table 14
Dependence of the Young's Modulus E_y on the FE beam model height.

Height variation						
Domain [Cells]	2 × 2 × 2	2 × 3 × 2	2 × 4 × 2	2 × 5 × 2	2 × 10 × 2	2 × 15 × 2
E_y [MPa]	345.7	347.3	348.1	348.6	350.0	350.6

Table 15
Dependence of the Young's Modulus E_y on the FE beam model width.

Section variation					
Domain [Cells]	3 × 2 × 3	4 × 2 × 4	5 × 2 × 5	10 × 2 × 10	15 × 2 × 15
E_y [MPa]	340.9	339.3	338.4	336.9	336.4

Table 16
Dependence of the Young's Modulus E_x on the FE beam model height.

Height variation						
Domain [Cells]	$2 \times 2 \times 2$	$3 \times 2 \times 2$	$4 \times 2 \times 2$	$5 \times 2 \times 2$	$10 \times 2 \times 2$	$15 \times 2 \times 2$
E_x [MPa]	274.2	275.5	276.2	276.6	277.8	278.2

Table 17
Dependence of the Young's Modulus E_x on the FE beam model width.

Section variation					
Domain [Cells]	$2 \times 3 \times 3$	$2 \times 4 \times 4$	$2 \times 5 \times 5$	$2 \times 10 \times 10$	$2 \times 15 \times 15$
E_x [MPa]	271.8	271.2	270.9	270.5	270.3

Table 18
Elastic properties of the beam model with increasing foam domain size.

Domain [Cells]	Ey [MPa]	E_x [MPa]	Ey/Ex [−]	ΔE_y beam-exp [%]	ΔE_x beam-exp [%]	$\Delta E_y/E_x$ beam-exp [%]
$3 \times 3 \times 3$	342.7	273.5	1.253	0.17	0.44	0.32
$9 \times 9 \times 9$	343.5	276.0	1.245	0.06	0.47	−0.32
$15 \times 6 \times 15$	343.6	276.4	1.243	0.09	0.62	−0.48
$30 \times 10 \times 30$	343.0	279.0	1.230	0.09	1.57	1.52
$30 \times 30 \times 30$	346.7	279.1	1.242	0.99	1.60	−0.56

Table 19
Computational burden of the solid model and beam model in terms of node and element numbers for the foam domain $3 \times 3 \times 3$.

	Solid Model	Beam Model	Δ[%]
Nodes	194818	7236	−96.29
Elements	99019	7560	−92.37

the connection node evaluated with beam and solid models.

Specifically, the goal was to especially contain the values on the main diagonal of the stiffness table, i.e. the ones that most contribute to the mechanical behavior because of their greater magnitude. As a consequence, in order to minimize the terms on the main diagonal, the objective functions of the calibration process are:

$$\min\left(\Delta K_{ii}^{bs}\right) \tag{9}$$

This minimization was performed considering three constraint equations statingthat the percentage difference between the elastic moduli and their ratio, evaluated by beam and solid models of a $3 \times 3 \times 3$ a foam domain, must be:

$$\Delta E_y \leq 3\% \qquad \Delta E_x \leq 3\% \qquad \Delta E_y/E_x \leq 3\% \tag{10}$$

The threshold value of 3% was established since it is the difference of these properties between the solid model and the experimental data, see Ref. (Fanelli et al., 2017).

Furthermore, the search for the optimal solution was performed through the progressive increase of the scaling factor F, i.e. the connection node of the beam model was made stiffer and the terms $\mathbf{\Delta K^{bs}}_{\mathbf{ii}}$ were subsequently reduced. The initial value considered for the minimization was $F = 1.0$, it was progressively increased, with step 0.5, until the concurrent fulfilment of the three constraint equations. As outlined in Table 10, as the scaling factor raises the percentage differences of the stiffness table are decreased. The calibration returned a scaling factor $F = 2.50$ as the first value capable of reaching the objective, i.e. minimizing the terms on the main diagonal of the stiffness tables and satisfying all the constraint equations; in fact, see Table 11, the percentage differences of the elastic moduli and their ratio are below the threshold value. Additionally, the new values of percentage difference between stiffness tables are reported in Table 12. It is possible to notice a relevant reduction of the percentage difference between the stiffness tables, except for some secondary terms out of the main diagonal whose effect on the overall foam domain elastic properties is negligible. To emphasize the differences with respect to Table 7, the improved values are outlined in green and the worsened ones in red.

As a further confirmation of the calibration suitability, the FE beam model of the $3 \times 3 \times 3$ foam domain was compared with the experimental outcomes. Table 13 shows the excellent results of the calibrated beam model compared with the experimental test in terms of elastic moduli and anisotropy factor.

7. Influence of foam domain dimensions on FE beam modeling

The investigation hereafter described regards the assessment of the FE beam model sensibility to the size of foam domain. Consequently, the results concerning the elastic moduli obtained with FE analyses performed on models with different foam domain dimensions are compared. In particular, the distinct variations of the height and width of the FE models were considered acting on the number of Kelvin cells composing the domain. As an example, two of the FE model samples employed for the sensibility analysis are shown in Fig. 11. The boundary conditions utilized to measure the two elastic moduli are showed in Fig. 11(a) and (b), they consist in simply supported.

As regards the Young's Modulus E_y, the obtained values are outlined in Tables 14 and 15 for height and width variations, respectively. It can be concluded that the measurement of this elastic property by means of the beam model is substantially independent from the foam domain size, as a matter of fact the differences of values are limited within the 3%.

Analogous considerations can be formulated for the modulus E_x whose values are reported in Tables 16 and 17. Also, in this case, a negligible dependence of the results on the size of the foam domain is observed.

Moreover, the stability of the beam model equivalent moduli and its anisotropy, in terms of E_y/E_x ratio, were also investigated increasing the foam domain dimensions, the determined values are depicted in Table 18. Results feature no significant variation of these properties; additionally, an excellent agreement with experimental estimations was observed.

The outcomes of the sensibility analysis further confirm both the capability of the FE beam modeling to analyze foam domains and the adequacy of the calibration process described in the previous Section.

In particular, the beam model estimation of the elastic properties demonstrates a very remarkable agreement with the experimental data. This result assures that the beam model features a calibrated compressive behavior along both the y- and x-directions and it can be employed for several engineering applications.

Furthermore, Table 19 provides a quantitative measure of the computational burden savings that can be attained by means of the foam beam model for a benchmark FE model consisting in 3x3x3 unit cells along the three Cartesian directions. As a matter of fact, the quantity of nodes and elements building up the model are drastically reduced passing from the solid to the beam model, this has a direct impact on the simulation time that is decreased of the 93%. Additionally, as previously remarked, no accuracy loss of the calibrated foam domain elastic property estimation is observed.

8. Conclusions

In this paper, a FE modeling approach for open-cell foams based on beam elements was outlined. The structural study consists in an experimental survey and in the development of a simulation technique for foams.

The modeling strategy exploits the geometry of the foam ligament profile defined in (Fanelli et al., 2017); the FE model was presented considering different alternatives for the beam elements cross-section. The solution with discrete variation of circular cross-section turns out to be the most appropriate to simulate the foam behavior observed with experimental evidence.

However, it was shown that a beam modeling purely based on the geometrical features of the foam returns a lower estimation of the elastic properties. In fact, differences in stiffness were determined between beam and solid models. This evidence is related to the FE beam modeling of the ligaments connection nodes which fails to reproduce the three-dimensional features of this zone.

This issue was solved assigning a different value of Young's Modulus to the material of the ligaments portion close to the connection nodes after a calibration process. Consequently, the difference in terms of structural behavior between the equivalent beam model and the solid model was strongly reduced. A sensibility analysis was performed to assess the effect of the foam domain size on the elastic properties determined with the beam model and no relevant effect was determined.

In conclusion, the FE beam modeling further showed excellent agreement with the experimental results, demonstrating its accuracy and feasibility in dealing with open-cell foams simulation; in addition, the computational burden required by the beam model is much lower than the solid model one.

Credit author statement

V. G. Belardi: Conceptualization, Methodology, Software, Validation, Investigation, Resources, Data curation, Writing – original draft, Writing – review & editing, Visualization. P. Fanelli: Conceptualization, Methodology, Validation, Resources, Writing – review & editing, Supervision. S. Trupiano: Conceptualization, Methodology, Software, Validation, Investigation, Resources, Data curation, Writing – original draft, Writing – review & editing, Visualization. F. Vivio: Conceptualization, Methodology, Validation, Resources, Writing – review & editing, Supervision, Project administration.

Declaration of competing interest

The authors declare that they have no known competing financial interests or personal relationships that could have appeared to influence the work reported in this paper.

References

Aakash, B., Sirui, B., Shields, M.D., Stavros, G., 2019. On the high-temperature crushing of metal foams. Int. J. Solid Struct. 174–175, 18–27.

Ashby, M., Evans, A., Fleck, N., Gibson, L., Hutchinson, J., Wadley, H., 2000. MetalFoams: A Design Guide. Butterworth-Heinemann.

Barnes, A.T., Ravi-Chandar, K., Kyriakides, S., Gaitanaros, S., 2014. Dynamic crushing of aluminum foams: Part I - Experiments. Int. J. Solid Struct. 51, 1631–1645.

Belardi, V.G., Fanelli, P., Vivio, F., 2018a. Structural analysis and optimization of anisogrid composite lattice cylindrical shells. Compos. B Eng. 139, 203–215.

Belardi, V.G., Fanelli, P., Vivio, F., 2018b. Design, analysisandoptimizationofanisogridcompositelatticeconicalshells, Composites Part B: Engineering 150, 184–195.

Belardi, V.G., Fanelli, P., Vivio, F., 2021. Theoretical definition of a new custom finite element for structural modeling of composite bolted joints. Compos. Struct. 258, 113199.

Cheng, Y., Liu, M., Zhang, P., Xiao, W., Zhang, C., Liu, J., Hou, H., 2018. The effects of foam filling on the dynamic response of metallic corrugated core sandwich panel under air blast loading - experimental investigations. Int. J. Mech. Sci. 145, 378–388.

Dabo, M., Roland, T., Dalongeville, G., Gauthier, C., KÃlkicheff, P., 2019. Ad-hoc modeling of closed-cell foam microstructures for structure-properties relationships. Eur. J. Mech. Solid. 75, 128–141.

Degischer, H., Brigitte, K., 2002. Handbook of Cellular Metals Production , Processing , Applications. Wiley-VCH Verlag GmbH & Co.

Duan, S., Xi, L., Wen, W., Fang, D., 2020. Mechanical performance of topology-optimized 3D lattice materials manufactured via selective laser sintering. Compos. Struct. 238, 111985.

Elsayed, M.S., Pasini, D., 2010. Multiscale structural design of columns made of regular octet-truss lattice material. Int. J. Solid Struct. 47, 1764–1774.

Fanelli, P., Evangelisti, A., Salvini, P., Vivio, F., 2017. Modelling and characterization of structural behaviour of Al open-cell foams. Mater. Des. 114, 167–175.

Gaitanaros, S., Kyriakides, S., 2014. Dynamic crushing of aluminum foams: Part II - Analysis. Int. J. Solid Struct. 51, 1646–1661.

Gong, L., Kyriakides, S., Jang, W.-Y., 2005. Compressive response of open-cell foams. Part I: morphology and elastic properties. Int. J. Solid Struct. 42, 1355–1379.

Guo, H., Takezawa, A., Honda, M., Kawamura, C., Kitamura, M., 2020. Finite element simulation of the compressive response of additively manufactured lattice structures with large diameters. Comput. Mater. Sci. 175, 109610.

Jang, W.-Y., Kraynik, A.M., Kyriakides, S., 2008. On the microstructure of open-cell foams and its effect on elastic properties. Int. J. Solid Struct. 45, 1845–1875.

Jin, N., Wang, F., Wang, Y., Zhang, B., Cheng, H., Zhang, H., 2019. Effect of structural parameters on mechanical properties of Pyramidal Kagome lattice material under impact loading. Int. J. Impact Eng. 132, 103313.

Jung, A., Diebels, S., 2017. Microstructural characterisation and experimental determination of a multiaxial yield surface for open-cell aluminium foams. Mater. Des. 131, 252–264.

Kulshreshtha, A., Dhakad, S., 2020. Preparation of metal foam by different methods: a review. Mater. Today: Proceedings.

Li, M., Lai, C., Zheng, Q., Han, B., Wu, H., Fan, H., 2019. Design and mechanical properties of hierarchical isogrid structures validated by 3D printing technique. Mater. Des. 168, 107664.

De Luca, R., Maviglia, F., Federici, G., Calabró, G., Fanelli, P., Vivio, F., 2019. Preliminary investigation on W foams as protection strategy for advanced FW PFCs. Fusion Eng. Des. 146, 1690–1693.

De Luca, R., Fanelli, P., Hunteler, C., Vivio, F., Calabró, M.F.Y.J.G., 2021. Comparison between finite element and experimental evidences of innovative W lattice materials for sacrificial limiter applications. Fusion Eng. Des., 112493

De Luca, R., Fanelli, P., Mingozzi, S., Calabró, G., Vivio, F., Maviglia, F., You, J., 2020. Parametric design study of a substrate material for a DEMO sacrificial limiter. Fusion Eng. Des. 158, 111721.

Luo, G., Xue, P., Sun, S., 2018. Investigations on the yield behavior of metal foam under multiaxial loadings by an imaged-based mesoscopic model. Int. J. Mech. Sci. 142–143, 153–162.

Mao, R., Lu, G., Wang, Z., Zhao, L., 2016. Large deflection behavior of circular sandwich plates with metal foam-core. Eur. J. Mech. Solid. 55, 57–66.

Mao, H., Rumpler, R., Göransson, P., 2020. An inverse method for characterisation of the static elastic Hooke's tensors of solid frame of anisotropic open-cell materials. Int. J. Eng. Sci. 147, 103198.

Maskery, I., Aremu, A., Parry, L., Wildman, R., Tuck, C., Ashcroft, I., 2018. Effective design and simulation of surface-based lattice structures featuring volume fraction and cell type grading. Mater. Des. 155, 220–232.

Meng, K., Chai, C., Sun, Y., Wang, W., Wang, Q., Li, Q., 2019. Cutting-induced end surface effect on compressive behaviour of aluminium foams. Eur. J. Mech. Solid. 75, 410–418.

Muller, A., Binder, M., Calabró, G., De Luca, R., Fanelli, P., Neu, R., Schlick, G., Vivio, F., You, J., 2020. Tailored tungsten lattice structures for plasma-facing components in magnetic confinement fusion devices. Mater. Today 39, 146–147.

Nguyen, N.V., Lee, J., Nguyen-Xuan, H., 2019. Active vibration control of GPLs-reinforced FG metal foam plates with piezoelectric sensor and actuator layers. Compos. B Eng. 172, 769–784.

Plocher, J., Panesar, A., 2019. Review on design and structural optimisation in additive manufacturing: towards next-generation lightweight structures. Mater. Des. 183, 108164.

Ptochos, E., Labeas, G., 2012. Elastic modulus and Poisson's ratio determination of micro-lattice cellular structures by analytical, numerical and homogenisation methods. J. Sandw. Struct. Mater. 14, 597–626.

Qi, C., Sun, Y., Yang, S., 2018. A comparative study on empty and foam-filled hybrid material double-hat beams under lateral impact. Thin-Walled Struct. 129, 327–341.

Ren, X., Xiao, L., Hao, Z., 2019. Multi-property cellular material design approach based on the mechanical behaviour analysis of the reinforced lattice structure. Mater. Des. 174, 107785.

Solyaev, Y., Lurie, S., Koshurina, A., Dobryanskiy, V., Kachanov, M., 2019. On a combined thermal/mechanical performance of a foam-filled sandwich panels. Int. J. Eng. Sci. 134, 66–76.

Vigliotti, A., Pasini, D., 2012. Stiffness and strength of tridimensional periodic lattices. Comput. Methods Appl. Mech. Eng. 229–232, 27–43.

Vivio, F., 2009. A new theoretical approach for structural modelling of riveted and spot welded multi-spot structures. Int. J. Solid Struct. 46, 4006–4024.

Wang, E., Li, Q., Sun, G., 2020. Computational analysis and optimization of sandwich panels with homogeneous and graded foam cores for blast resistance. Thin-Walled Struct. 147, 106494.

Yang, C., Kyriakides, S., 2019. Multiaxial crushing of open-cell foams. Int. J. Solid Struct. 159, 239–256.

Yang, Y., Shan, M., Zhao, L., Qi, D., Zhang, J., 2019. Multiple strut-deformation patterns based analytical elastic modulus of sandwich BCC lattices. Mater. Des. 181, 107916.

Yang, H., Li, Y., Yang, Y., Chen, D., Zhu, Y., 2020. Effective thermal conductivity of high porosity open-cell metal foams. Int. J. Heat Mass Tran. 147, 118974.